Diagnosing hot-spot symmetry in surrogate ignition experiments via secondary DT-neutron spectroscopy at the NIF

P. J. Adrian,[1, a)] R. Bionta,[2] D. Casey,[2] M. Gatu Johnson,[1] S. Kerr,[2] B. Lahmann,[2] C. K. Li,[1] R. Nora,[2] R. D. Petrasso,[1] G. Rigon,[1] D. Schlossberg,[2] F. H. Séguin,[1] and J. A. Frenje[1]
[1)] *Plasma Science and Fusion Center: MIT, Cambridge, MA 02139*
[2)] *Lawrence Livermore National Laboratory, Livermore, CA 94550*

(Dated: 10 May 2024)

The directional energy spectrum of neutrons generated from the in-flight fusion reaction of 1-MeV Tritons contain information about the hot-spot symmetry. The National Ignition Facility (NIF) fields Symmetry Capsule (Symcap) implosions which have historically measured the symmetry of the radiation drive by measuring the hot-spot shape via x-ray self-emission. Symcaps are used to tune the hot-spot symmetry for ignition experiments at the NIF. This work shows the relationship between directional secondary DT-n spectra and x-ray imaging data for a large data base of Symcap implosions. A correlation is observed between the relative widths of the DT-n spectra measured with nTOFs and the shape measured with x-ray imaging. A Monte Carlo model which computes the directional secondary DT-n spectrum is used to interpret the results. A comparison of the x-ray and secondary DT-n data with the Monte Carlo model indicates 56% of the variance between the two data sets is explained by a P2 asymmetry. More advanced simulations using HYDRA suggest that the unaccounted variance is due to $P1$ and $P4$ asymmetries present in the hot spot. The comparison of secondary DT-n data and x-ray imaging data to the modeling shows the DT-n data contains important information that supplements current $P2$ measurements and contains new information about the $P1$ asymmetry.

I. INTRODUCTION

Precision symmetry control over the stagnating fuel is essential for optimal energetics in Inertial Confinement Fusion (ICF). Asymmetries degrade the conversion of shell kinetic energy to hot-spot internal energy, compromising the energy confinement[1]. Studies have elucidated the adverse impact of low-mode asymmetries on key performance parameters such as hot spot temperature, areal density, and pressure[2–5]. Recent experiments in the burning plasma regime have shown that the yield is degraded by 50% for mode-2 amplitudes deviating from the highest yield implosion by 25%[6].

The National Ignition Facility (NIF) utilizes both time-resolved[7,8] and time-integrated[9,10] x-ray imaging diagnostics to assess implosion symmetry. A radiation drive asymmetry, caused by the expansion of gold plasma in the hohlraum, imprints a Legendre mode-2 ($P2$) asymmetry on the forming hot spot[11]. This drive asymmetry is seeded during the ablation of the hohlraum because the expansion of the gold-hohlraum plasma impedes the propagation of the lasers causing an imbalance in energy delivered to the waist of the hohlraum leading to a radiation drive asymmetry[11–13]. This asymmetry causes both a decrease in energy coupled to the hot spot and residual bulk flows which break confinement.

The Symcap technique implodes surrogate ignition targets, which replace the DT ice layer with an equivalent mass of ablator material and the DT vapor with a mixture of D_2 and D^3He gas. The Symcap implosion is used to study the radiation drive asymmetry of a hohlraum design. Throughout many Symcap experiments, an empirical scaling was established by Callahan[11]. This relation showed that the P2 asymmetry is proportional to the size of the bubble, the size of the hohlraum (R_{hohl}), and the capsule size (R_{cap}). The exact relationship is

$$P2 - 2.7 \times (CF - 33) = \sqrt{\frac{E_{picket,outer}}{A_{outer}\rho_{fill}}}\frac{\tau_{laser}}{R_{hohl}}\frac{R_{cap}}{R_{hohl}} - 1.2, \quad (1)$$

where CF is the cone fraction [%], $E_{picket,outer}$ is the energy [J] of the picket in the outer beams, A_{outer} is the hohlraum area [mm] that the outer beams illuminate, ρ_{fill} is the hohlraum gas fill density [mg/cc], and τ_{laser} is the pulse duration [ns]. This empirical relation facilitated the use of larger R_{cap} while offsetting the P2 asymmetry by modifying the other parameters. Equation 1 and the supporting data are used extensively in hohlraum design and have guided the HYBRID implosion campaign[14], which achieved ignition in the laboratory.

Although the Callahan relation has had tremendous success in guiding mitigation strategies of the

[a)] Author to whom correspondence should be addressed:pjadrian@lanl.gov

observed P2 asymmetry from x-ray imaging in Symcap implosions, questions persist about the accuracy of x-ray imaging in capturing the symmetry of the fissionable material. X-ray diagnostics, while providing valuable information, may face accuracy challenges due to localized mix regions distorting images[8,15]. Interpreting the shape information from x-ray self-emission images was a significant challenge in early experiments at the NIF, where high-intensity emission was observed in the imploded cores of ignition experiments. This localized emission was due to the fill tube injecting high-Z ablator material into the implosion core[16]. Techniques were developed to measure the underlying low-intensity hot-spot shape from the dominant high-intensity localized mix feature. Another, issue is that the hot-spot x-ray self-emission of a Symcap is faint because they are lower-convergence implosions. Furthermore, simulation studies have concluded that mode-4 asymmetries can manifest as mode-2 asymmetries in x-ray imaging leading to a misinterpretation of hot-spot shape[17]. All of the aforementioned issues introduce uncertainty in the shape measurements form x-ray imaging.

This paper details an alternative methodology for diagnosing hot spot asymmetry independent of x-ray self-emission imaging. Specifically, the use of neutron spectroscopy of secondary DT-neutrons is advanced as a diagnostic to assess the hot-spot symmetry. Symcaps produce an appreciable amount of secondary DT fusion reactions from the in-flight reaction of the triton emitted from the DD reaction. The reaction chain is

$$\mathrm{D} + \mathrm{D} \rightarrow \mathrm{p}\ (3.02\ \mathrm{MeV}) + \mathrm{T}\ (1.01\ \mathrm{MeV}) \quad (2)$$

$$\mathrm{D} + \mathrm{T}\ (< 1.01\ \mathrm{MeV}) \rightarrow \mathrm{n} + \alpha. \quad (3)$$

Secondary DT-n spectroscopy has previously provided critical information about ρR, T_e, and mix[18]. Several key advancements in nTOF architecture[19,20] and larger yields at the NIF enabled unprecedented measurements of secondary DT-n spectra. The first measurements demonstrating the dependence of the shape of directional secondary DT-n energy spectra and the hot-spot symmetry were detailed by Cerjan[21]. This was followed up with an extensive study demonstrating the systematic imprint of mode-2 asymmetries on the secondary DT-n spectra[22]. Previous work by Cerjan[21] and Lahmann[22] established the impact of low-mode hot-spot asymmetries on the shape of the secondary DT-n spectra.

Directional secondary DT-n spectroscopy is also an important diagnostic for Magneto-Inertial Fusion experiments[23,24]. In this context, the compressed magnetic field changes the escape path of the DD-triton due to the gyro motion, which impacts both the yield and directional neutron spectra. Measurements of secondary DT-n spectra are used to infer the magnetization of the fuel, which is a critical performance metric[25–28]. In addition, magnetized indirect-drive implosion experiments[29] at the NIF have also examined secondary DT-n production to diagnose the strength of the compressed magnetic field[30].

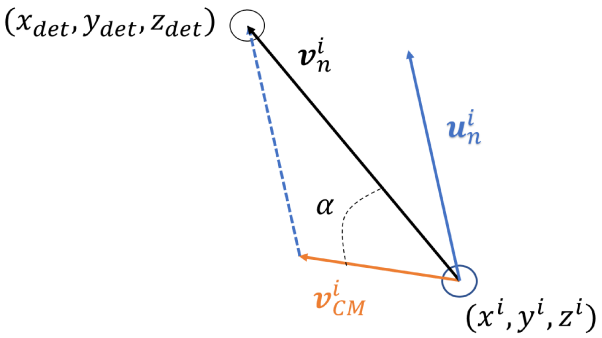

FIG. 1. Illustration showing the vector addition of $\mathbf{v}_{CM}^i$, $\mathbf{u}_n^i$, and $\mathbf{v}_n^i$. This velocity addition is used to compute $\mathbf{v}_n^i$ in the laboratory frame so that the neutron is detected at a given detector coordinate (x^i, y^i, z^i).

This work substantially advances previous studies, discussed in Refs 22 and 21, by contrasting and discussing the hot-spot asymmetry data, derived from directional secondary DT-neutron spectra, to x-ray imaging data for sixty SymCap implosions. This work also goes beyond previous studies by providing a detailed comparison of the asymmetry data, derived from the secondary DT-neutron and x-ray data, to HYDRA simulations.

This paper is composed as follows. Section II describes the modeling of the secondary DT-n data obtained at the NIF using Monte Carlo simulation techniques. Section III describes the nTOF architecture at the NIF used to measure secondary DT-neutrons emitted from implosions. It also describes the experimental database used in this work. Section IV describes the analysis applied to the entire data set as well as trends observed in the data. Section V describes data linking observations in the direction emission spectrum from secondary DT-n and the shape of the hot spot. Section VI concludes and summarizes the results.

II. MODEL OF DIRECTIONAL NEUTRON SPECTRUM

A Monte Carlo simulation tool was developed to compute the directional secondary DT-n spectra from a hot spot with uniform profiles. The Monte Carlo transport code is initialized by defining a hot spot boundary, $R(\theta)$, where θ is the polar angle in

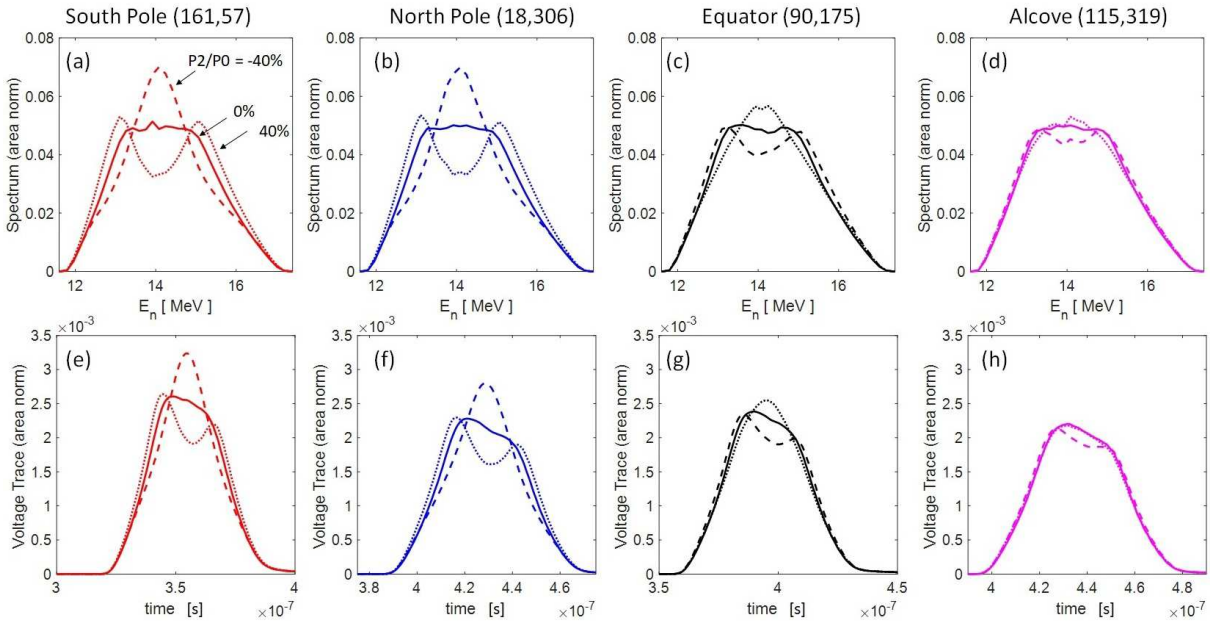

FIG. 2. The upper row shows example emission spectra emitted in the direction of the South Pole (a), North Pole (b), Equator (c), and Alcove (d) computed from the Monte Carlo model for a hot-spot $\rho R = 100$ mg/cm^2, $T_e = T_i = 4$ keV. Each figure shows results for a hot spot with a P2/P0 = -40% (dashed), 0% (solid), and +40% (dotted) asymmetry. The lower row shows simulated nTOF traces using the computed spectra in the upper row and the measured IRF. The time basis in (e-h) accounts for the time-of-fight to each detector and assumes all DT-n productions occurs at time = 0 ns. The (θ, ϕ) coordinates for each detector are labeled in the column titles.

shperical coordinates. For this work, the boundary is defined by

$$R(\theta) = P0 + P2\left(\frac{3}{2} - \frac{1}{2}\cos^2(\theta)\right) \tag{4}$$

where $P0$ and $P2$ are the Legendre coefficients. Tritons are uniformly sourced throughout the interior of the boundary with initial positions at time step 0 of (x^0, y^0, z^0), and are not tracked once they leave the boundary. The simulation is initialized with N=10^4 tritons within the volume. The initial velocity vector of a particle (v_x^0, v_y^0, v_z^0) is sampled to be isotropic. However, the velocity magnitudes are chosen such that the DD-t energy distribution obeys

$$f_T(E^i) = exp\left(\frac{(E_i - \Delta E_{th}(T_D))}{\sigma_{th}^2(T_D)}\right) \tag{5}$$

where $\Delta E_{th}(T_D)$ and $\sigma_{th}^2(T_D)$ are computed from the nuclear kinematics[31]. The positions and velocities of the tritons are advanced using a Verlet integration method. The $(i+1)$-th positions are updated according to

$$x^{i+1} = x^i + v_x^i \delta t + 0.5(\delta t)^2 a_x^i \tag{6}$$
$$y^{i+1} = y^i + v_y^i \delta t + 0.5(\delta t)^2 a_y^i \tag{7}$$
$$z^{i+1} = z^i + v_z^i \delta t + 0.5(\delta t)^2 a_z^i. \tag{8}$$

The velocities in the labratory frame are advanced as,

$$v_x^{i+1} = v_x^i + a_x^i \delta t \tag{9}$$
$$v_y^{i+1} = v_y^i + a_y^i \delta t \tag{10}$$
$$v_z^{i+1} = v_z^i + a_z^i \delta t \tag{11}$$
$$, \tag{12}$$

where the acceleration is taken to be due to the plasma stopping and slowing down of the triton, which is given by,

$$a_x^i = \frac{1}{m_T}\frac{v_i^x}{|v|^i}\frac{dE}{dx}(E_i, n_{ei}, T_{ei}) \tag{13}$$
$$a_y^i = \frac{1}{m_T}\frac{v_i^y}{|v|^i}\frac{dE}{dx}(E_i, n_{ei}, T_{ei}) \tag{14}$$
$$a_z^i = \frac{1}{m_T}\frac{v_i^z}{|v|^i}\frac{dE}{dx}(E_i, n_{ei}, T_{ei}), \tag{15}$$

where dE/dx is the stopping power. This work uses the BPS stopping power model[32] which has been recently validated for DD-t stopping in HEDP plasmas[33]. The distance traveled by each triton during a single time step is given by

$$d\ell^{i+1} = \sqrt{(x^{i+1} - x^i)^2 + (y^{i+1} - y^i)^2 + (z^{i+1} - z^i)^2}. \tag{16}$$

At every time step, every DD-t in the Monte Carlo simulation produces one DT-n. However, the DT-n produced at the i-th time step is assigned a weight w^i equal to the probability P^i of it being created. If the simulation is run for M time steps and tracks N particles, the final number of neutrons produced is $N \times M$. The probability of a DD-t reacting with the background deuterium is given by[18]

$$P^{i+1} = n_D^{i+1}\sigma_{DT}\Big(\frac{1}{2}\frac{m_T m_D}{m_D+m_T}|\mathbf{v}_{CM}^i|^2\Big)\times d\ell^{i+1}\left(1-\sum_{k=1:i}P^k\right). \quad (17)$$

The weights of every neutron are saved and used in the computation of the final output neutron spectrum. To compute the probability at every time step, the code computes the center-of-mass velocity, $\mathbf{v}_{CM}^i$, assuming the DD-t interacts with an ambient deuteron. The deuteron velocity vector in the laboratory frame, $\mathbf{v}_D$, is statistically sampled to be isotropic in direction and the velocity magnitude is sourced from a Maxwellian speed distribution of temperature T_D. Thus, the center-of-mass velocity of the reaction in the laboratory frame is given by

$$\mathbf{v}_{CM}^i = \frac{m_D\mathbf{v}_D + m_T\mathbf{v}^i}{m_D+m_T}. \quad (18)$$

The birth energy of the i-th neutron is expressed as

$$E_n^i = E_n^0 + \frac{1}{2}\frac{m_\alpha}{m_\alpha+m_n}\frac{m_D m_T}{m_D+m_T}|\mathbf{v}_D-\mathbf{v}^i|^2. \quad (19)$$

The birth velocity vector in the center-of-mass frame, $\mathbf{u}_n^i$, is subsequently constructed to have an isotropic emission distribution[34] with a magnitude $\frac{1}{2}m_n(u_n^i)^2 = E_n^i$. The Monte Carlo code generates the spectrum of secondary DT-n at a specific detector, which is assumed to be a point at a location $(x_{Det}, y_{Det}, z_{Det})$. The birth velocity, $\mathbf{u}_n^i$ and center-of-mass velocity, $\mathbf{v}_{CM}^i$, must add up to enable the neutron to pass through the detector at $(x_{Det}, y_{Det}, z_{Det})$ from the reaction's position at (x^i, y^i, z^i). Figure 1 shows the relationship between the three vectors $\mathbf{v}_{CM}^i$, $\mathbf{v}_n^i$, and $\mathbf{u}_n^i$. The magnitude of the DT-n velocity, $\mathbf{v}_n^i$, vector is computed from the law of cosines as

$$0 = |\mathbf{v}_n^i|^2 - 2|\mathbf{v}_{CM}^i||\mathbf{v}_n^i|\cos\alpha + |\mathbf{v}_{CM}^i|^2 - |\mathbf{u}_n^i|^2, \quad (20)$$

where the angle α is given by

$$\cos\alpha = \hat{\mathbf{v}}_n \cdot \hat{\mathbf{v}}_{CM}^i, \quad (21)$$

where the hat symbol denotes unit vectors. Equation 20 is solved using the quadratic formula for $\mathbf{v}_n^i$ as,

$$|\mathbf{v}_n^i| = |\mathbf{v}_{CM}^i|\cos\alpha + \sqrt{|\mathbf{v}_{CM}^i|^2(\cos^2(\alpha)-1) + |\mathbf{u}_n^i|^2} \quad (22)$$

The final energy of the neutron is simply $E_n^i = \frac{1}{2}m_n|\mathbf{v}_n^i|^2$. However, weights must be assigned to account for artificially forcing the neutrons to be emitted into the detector. To correct for this effect the weight assigned to each neutron is

$$\mathcal{W}^i = \frac{E_n^i}{\frac{1}{2}m_n|\mathbf{u}_n|^2}. \quad (23)$$

A detailed explanation of this weighting scheme, which corrects for the reference frame effects on neutron production, is found in Appendix B of Knapp *et al*[26]. The spectrum emitted into the detector is thus a histogram of neutron energies, E_n^i, where each tally is weighted by $w^i \times \mathcal{W}^i$.

The low-mode asymmetry of the hot spot imprints structure on the directional DT-n spectra[21,22]. Figure 2 displays the characteristic effect of a mode-2 asymmetry on the emitted spectra along the four nTOF directions (detailed in Section III), as computed by the model presented above. For example, an oblate implosion (negative P2) produces secondary DT-n spectra emitted in the polar direction that peaks around 14.07 MeV, the birth energy of the DT-n. The oblate shape causes there to be a higher areal density along the equator, which increases the probability that a neutron will be emitted from a triton traveling perpendicular to the detector. Thus, the polar nTOF detectors preferentially detect neutrons emitted with smaller Doppler shift. Spectra for a P2/P0 = -40% hot spot is shown in Figure 2 (a) and (b) for the south and north pole detector directions. Conversely in the equatorial direction, the spectra has peaks close to the minimum and maximum allowed kinetic energy. This is because it is more probable that tritons are traveling parallel to the detector and thus Doplar shifting the detected neutrons. This effect is shown in Figure 2 (c) for the equatorial detector. For prolate implosions (positive P2) the effect is the opposite as illustrated in Figure 2 (a-c). Interestingly, the alcove detector is positioned at an angle such that the P2 asymmetry of the hot spot has minimal impact on the emitted spectra. In this direction, there is predicted to be little difference on the observed spectra.

In this paper, the model described above is the Monte Carlo model (MCM) and it computes the directional secondary DT-n spectra in asymmetric hot spots. The MCM also computes the predicted nTOF signal trace. This signal trace is computed through a convolution of the emitted spectrum with the instrument response accounting for the time-of-flight.

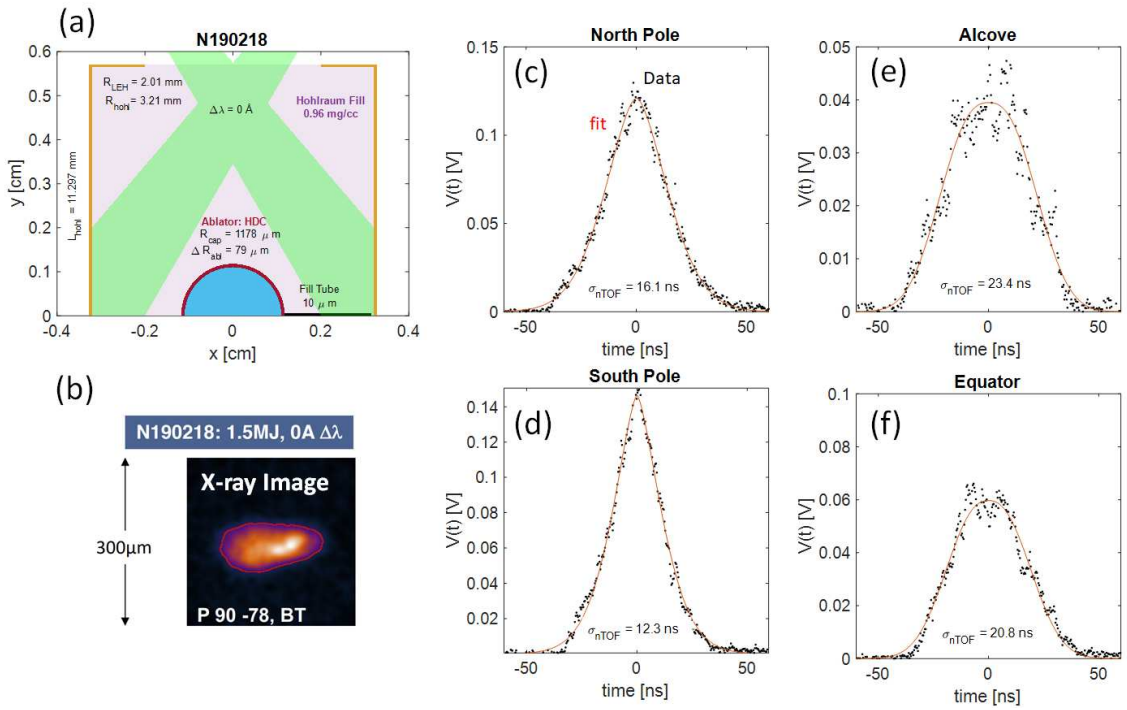

FIG. 3. (a) Depiction of the SymCap HyE capsule and hohlraum for shot N190218. Indicated are the hohlraum length (L_{hohl}), inner radius (R_{hohl}), laser entrance hole (R_{LEH}), capsule outer radius (R_{cap}), HDC thickness (ΔR_{abl}), fill tube size, hohlraum fill density, and the wavelength shift between inner and outer beams ($\Delta\lambda$). The total laser energy delivered was 1.5 MJ. (b) X-ray image recorded on the equatorial DIM along the θ=90^o, ϕ=78^o axis at bang time. Secondary DT-n signal trace for the (c) north pole, (d) south pole, (e) alcove, (f) equator nTOFs. Fits to the nTOF spectra using Equation 25 are shown. The widths of the spectra (σ_{nTOF}) are also given.

The nTOF trace is computed as[35]

$$V_{MC}(t) = \int_0^t Y_{DT}(E(t))\frac{dE}{dt} IRF(t,E)dt, \qquad (24)$$

where $Y_{DT}(E(t))$ is the number of neutrons emitted in energy window $E + dE$ (computed from the MCM), $IRF(t,E)$ is the instrument response function. The light output as a function of neutron energy[36] and instrument response as a function of time[20] of each detector have been extensively characterized and used to compute $IRF(t,E)$. The energy to time conversion is computed as $E(t) = m_n c^2(1/\sqrt{1-(R_{det}/ct)^2} - 1)$ where m_n is the neutron mass and c is the speed of light. Figure 2 (e-h) shows the computed nTOF signal trace as a function of time for each spectra presented in (a-d).

III. EXPERIMENTS AND DATA ANALYSIS

The experiments constituting this work are a series of Symcap implosions at the NIF. A total of 60 Symcap implosions were identified over the years 2016 to 2022 as having high-quality secondary DT-n data. These experiments tested the impact of several hohlraum and capsule design choices on the radiation drive symmetry. Table II details a list of the experiment shot numbers, campaign names, and data. Each experiment produced x-ray self-emission imaging data that was acquired by either time-integrated[10,37] or time-resolved imaging[7]. The images were taken along an equatorial line-of-sight to diagnose the polar symmetry of the hot spot. The imaging data was reduced to provide a P0 and P2 for each implosion.

Detector:	NP	SP	E	A
θ [^{o}]	18	161	90	115
ϕ [^{o}]	306	57	175	319
R_{det} [m]	21.61	17.98	20.09	22.22

TABLE I. Spherical coordinates (R_{det}, θ, ϕ) for each nTOF system used in this work.

The primary detectors for measuring secondary DT-n spectra were four nTOF systems[38]: 18m SPEC-South Pole (SP), 21m SPEC-North Pole (NP), 20m SPEC-Equator (E), 20m SPEC-Alcove (A). Table I shows the detector radius (R_{det}), polar

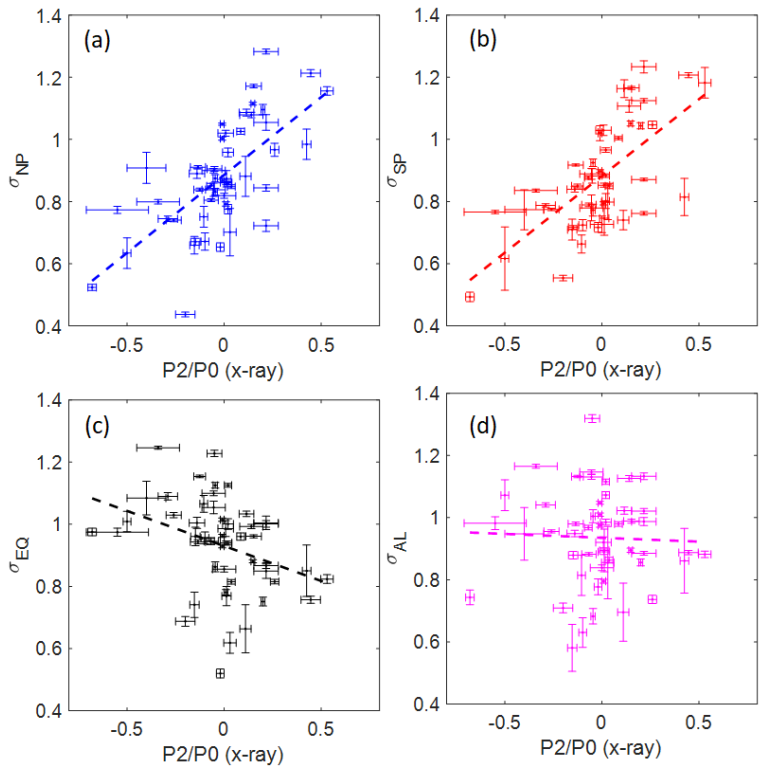

FIG. 4. Summary of 60 Symcp experiments for (a) σ_{NP}, (b) σ_{SP}, (c) σ_{EQ}, and (d) σ_{AL} as a function of P2/P0. Each figure also has a best-fit line to the guide the eye to the trends observed in each case.

(θ), and azimuthal (ϕ) coordinates of each detector system.

One example from the data set is shown in Figure 3. The hohlraum and capsule design is shown in Figure 3(a). This experiment was a part of the symmetry tuning campaign for the Hybrid-E campaign[39,40]. The x-ray image shown in Figure 3 (b) was highly oblate with a P2/P0 = -41%, which was due to the design testing a larger capsule. The larger capsule enhanced the capsule-to-hohlraum size ratio, which caused the gold bubble to block the inner beams more and decrease compression along the equator, which was predicted by the Callahan model. Figure 3 (c-f) shows secondary DT-n nTOF traces for the four nTOF systems. The time basis for each trace is shifted so that each trace centered at the emission averaged mean. Visually, the directional time-of-flight voltage traces also show an asymmetry in their widths, where the detectors on the poles measure a narrower distribution than the equatorial detectors.

IV. ANALYSIS OF EXPERIMENTAL DATA FROM SYMCAP IMPLOSIONS

The MCM shows that the P2 asymmetry is encoded in the relative width of the polar versus equatorial nTOF traces. This is also empirically seen in the sample data provided in the previous section. To systematically examine this trend across the data base, a voltage model for the nTOF signal traces was adapted from Lahmann in Ref. [22]. This model quantifies the width of the nTOF voltage trace as

$$V(t) = \frac{A}{2w\Gamma((n+1)/n)} \exp\left(- \left| \frac{t-\tau}{w} \right|^n \right), \quad (25)$$

where A sets the amplitude, w is related to the width, n controls the 'peakedness', and τ sets the average arrival time. The standard deviation of the signal is given by

$$\sigma_{nTOF} \equiv w(\ln 2)^{1/n}. \quad (26)$$

Figure 3 (c-f) displays example fits of this model to the nTOF traces for each of the four detectors. Also indicated in the figure is the σ_{nTOF} for each trace. The empirical voltage trace model (Eq. 25)

was used instead of the full forward model (Eq. 24) due to uncertainties in the absolute timing of the nTOFs over the large data base, which prevented reconstruction of the energy spectra.

The nTOF detectors are positioned at different distances from the implosion which causes different time-of-flight broadening. The change in widths of the direction secondary DT-n voltage trace due to hot-spot asymmetry is assessed by correcting for the time-of-flight broadening difference between the detectors. First, each trace is fit using Eq. 25 to determine σ_{nTOF}. Then, σ_{nTOF} is corrected by dividing by the detector distance, R_{det}. The explicit formulas for each detector are given by

$$\sigma_{NP} = \sigma_{nTOF}/21.61, \quad (27)$$
$$\sigma_{SP} = \sigma_{nTOF}/17.98, \quad (28)$$
$$\sigma_{EQ} = \sigma_{nTOF}/20.09, \quad (29)$$
$$\sigma_{AL} = \sigma_{nTOF}/20.61. \quad (30)$$

The sensitivity of the TOF width to the hot-spot asymmetries is observed in the data. The entire 60-shot data set was analyzed using the voltage model above to extract σ_{NP}, σ_{SP}, σ_{EQ}, and σ_{AL} for each shot. The results of this analysis are summarized in Figure 4 which shows the widths of each nTOF trace versus the P2/P0 asymmetry as measured by x-ray self-emission imaging. Also shown in Figures 4 (a-d) are best fit linear trend lines to the data. These fits guide the observation that the widths of the polar nTOF traces are positively correlated with the observed P2 asymmetry, while the equatorial widths are negatively correlated. However, there is no correlation observed with the Alcove detector. These observations are consistent with the MCM discussed above and illustrated in Figure 2 (e-h).

V. COMPLIMENTARY SHAPE MEASUREMENTS UTILIZING SECONDARY DT-N SPECTRA

Even though there exist global trends pertaining to the individual TOF widths as a function of hot-spot P2, the individual widths are affected by the details of the implosion. Notably, the ρR of the implosion impacts the energy spectrum width[41,42]. For the data set presented, the hot-spot ρR varied from 20 to 100 mg/cm^2 over the entire data set. The MCM computed σ_{EQ}/σ_{NP} as a function of $P2$ for a hot-spot ρR spanning range observed in the experiments. Figure 5 displays the MCM results for $\rho R = 50$ mg/cm^2 (solid red curve) and the shaded red region represents the max-to-min model variation spanning $\rho R = 20$ to 100 mg/cm^2. The variation due to ρR is a 5% effect on the predicted trend for σ_{EQ}/σ_{NP} as a function of $P2$, which implies that

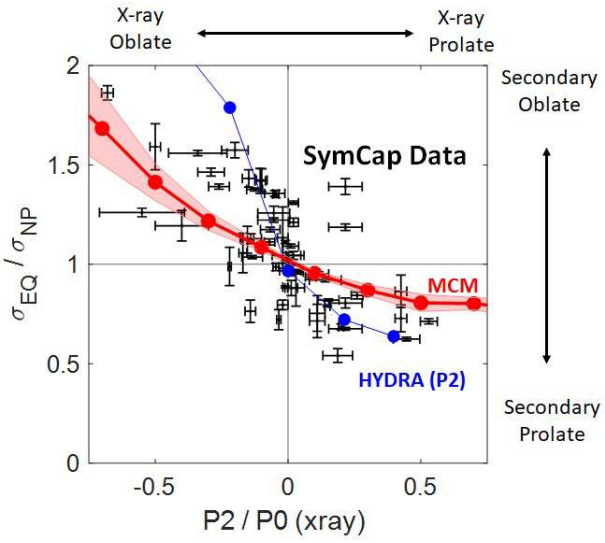

FIG. 5. Summary of SymCap measured σ_{EQ}/σ_{NP} as a function of $P2/P0$ determined from measured x-ray images (black). Predictions for the correlation using the Monte Carlo transport model (solid red curve) for an implosion with a hot spot $\rho R = 50$ mg/cm^2. The red-shaded region depicts the variations in the MCM for hot-spots with ρR from 20 to 100 mg/cm^2. HYDRA predicted scaling including only simulations with P2 hot-spot asymmetries (blue dashed curve).

the ρR effects can be mitigated by examining the ratio of the polar to equatorial widths.

Figure 5 presents the relationship between σ_{EQ}/σ_{NP} and $P2/P0$, as determined from DT-n data and x-ray imaging data. A more pronounced correlation is observed between the nTOF data and x-ray data, where the implosions displaying $\sigma_{EQ} > \sigma_{NP}$ are diagnosed to be oblate in x-ray imaging and the reverse for prolate implosions. This observed trend is consistent with predictions using the Monte Carlo code. The coefficient of determination, or R^2[43], was calculated to quantify the variations observed in the data and the variation predicted by the MCM. The R^2 metric indicates that 56% of the variance observed in the data is explained by the P2 asymmetry as predicted by the MCM. This suggests that the majority of the observed trends are due to the underlying P2 asymmetry of the hot spot.

A. HYDRA Simulations

While the majority of the variance observed in the secondary nTOF data can be explained by the P2 asymmetry of the hot spot, a substantial fraction is potentially from other sources. A series of 125 HYDRA[44] simulations were conducted to fur-

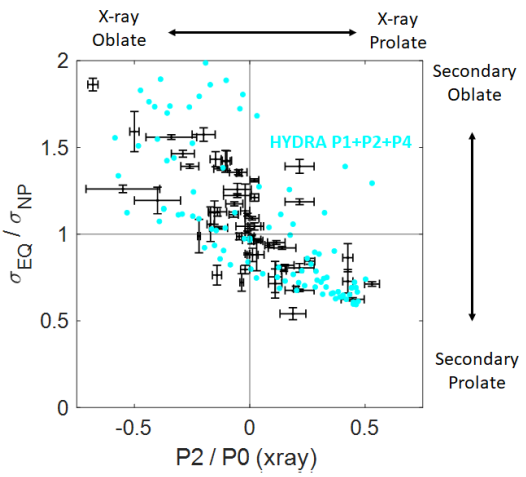

FIG. 6. Variation predicted by HYDRA when including P1, P2, and P4 low-mode asymmetries (cyan). The variations predicted by HYDRA from P1, P2, and P4 asymmetries appear to match the spread in the data suggesting that those asymmetries are present in the implosions.

ther explore the unaccounted variance observed in this data set. HYDRA was initialized in 2-D cylindrical geometry. The simulation considered a radiation drive incident upon an HDC ablator. Asymmetry was introduced by perturbing the x-ray drive on the capsule with P1, P2, and P4 perturbations. The P1, P2, and P4 amplitude was varied in five steps of -5, -2.5, 0, 2.5, and 5% for a total number of 125 simulations to explore all combinations. Five simulations exclusively examined the P2 asymmetry.

Calculations of the secondary DT-neutron spectra emitted towards the north Pole and Equator nTOF detectors were performed for all 125 simulations. Each simulation also produced an x-ray image from which the shape of the hot spot was inferred. The major difference besides the inclusion of P1 and P4 asymmetry is that the HYDRA simulations include temporal evolution and realistic density and temperature profiles when generating the secondary DT-n spectra.

The HYDRA simulations predicted a different scaling for the correlation between σ_{EQ}/σ_{NP} and $P2$. This suggests some of the scatter in the data could be due to the time evolution or the profile effects of the DT-n emission.

Another source of scatter in the data is potentially from $P1$ and $P4$ asymmetries. Figure 6 shows the same data but overlaid with the results of the 125 HYDRA simulations with a mix of $P1$, $P2$, and $P4$ asymmetries. The trends observed in the HYDRA simulations suggest that a majority of the scatter in the data is attributable to an interplay of multiple low-mode asymmetries. The P1 asymmetry is not measured in Symcap implosions as the x-ray imaging systems are not absolutely calibrated to determine the center of the hot spot. This asymmetry is primarily caused by a top-drown asymmetry in the radiation drive. Diagnosing the P1 asymmetry in Symcaps can potentially identify systematic mode-1 asymmetries. This could be used to test mode-1 mitigation strategies using the more economical Symcap platform as opposed to ignition experiments.

VI. CONCLUSIONS

In conclusion, an alternative method to diagnose hot-spot symmetry utilizing the directional emission spectra of secondary DT-n reaction is shown to contain hot-spot shape data. A large database of secondary DT-n measurements and x-ray measurements was leveraged to explore the relationship between secondary DT-n data and x-ray data. The observed trends were supported by both Monte-Carlo modeling and detailed radiation-hydrodynamics simulations of the triton transport. The results suggest that a combination of x-ray and secondary DT-n provides critical hot-spot symmetry information in surrogate ignition targets.

Generally, the secondary DT-n data supplements x-ray imaging data when determining the $P2$ of an implosion. The secondary DT-n data also has additional information about the $P1$ and $P4$ asymmetries. Information on P1 asymmetries are difficult to diagnose in SymCap implosions. Typically P1 asymmetries can only be diagnosed ignition experiments where there is sufficient primary DT-n yield to measure the bulk flow vector of the hot spot. However, this study only suggests secondary DT-n spectroscopy contains information about the P1 asymmetry of the radiation drive. Future work will be need to find a quantitative methodology for inferring a P1 asymmetry from the measurements.

Overall, secondary DT-n spectroscopy is shown to contain important information that supplements the current shape measurements at the NIF. This data can be leveraged when evaluating the performance of the radiation drive of ignition-relevant designs at the NIF.

ACKNOWLEDGMENTS

This work was supported in part by DOE/NNSA CoE under Contract No. DE-NA0003868 and the LLNL under Contract No. B640112; P. J. Adrian was supported by NNSA SSGF under Contract No. DE-NA0003960.

DATA AVAILABILITY STATEMENT

The data that support the findings of this study are available from the corresponding author upon reasonable request.

[1]D. T. Casey, D. B. Sayre, C. R. Brune, V. A. Smalyuk, C. R. Weber, R. E. Tipton, J. E. Pino, G. P. Grim, B. A. Remington, D. Dearborn, L. R. Benedetti, J. A. Frenje, M. Gatu-Johnson, R. Hatarik, N. Izumi, J. M. McNaney, T. Ma, G. A. Kyrala, S. MacLaren, J. Salmonson, S. F. Khan, A. Pak, L. B. Hopkins, S. LePape, B. K. Spears, N. B. Meezan, L. Divol, C. B. Yeamans, J. A. Caggiano, D. P. McNabb, D. M. Holunga, M. Chiarappa-Zucca, T. R. Kohut, and T. G. Parham, Nature Physics **13**, 1227 (2017), number: 12 Publisher: Nature Publishing Group.

[2]O. A. Hurricane, D. T. Casey, O. Landen, A. L. Kritcher, R. Nora, P. K. Patel, J. A. Gaffney, K. D. Humbird, J. E. Field, M. K. G. Kruse, J. L. Peterson, and B. K. Spears, Physics of Plasmas **27**, 062704 (2020).

[3]O. A. Hurricane, D. T. Casey, O. Landen, D. A. Callahan, R. Bionta, S. Haan, A. L. Kritcher, R. Nora, P. K. Patel, P. T. Springer, and A. Zylstra, Physics of Plasmas **29**, 012703 (2022).

[4]K. M. Woo and R. Betti, **28**, 054503.

[5]R. C. Nora, N. Birge, D. Casey, C. Danly, E. L. Dewald, B. Z. Djordjevic, A. Do, M. Durocher, J. E. Field, D. Fittinghoff, M. S. Freeman, J. Gaffney, V. Geppert Kleinrath, S. Haan, K. Hahn, E. Hartouni, M. Hohenberger, S. Kerr, O. L. Landen, J. Milovich, A. S. Moore, P. Patel, D. J. Schlossberg, S. M. Sepke, B. K. Spears, P. L. Volegov, and C. Wilde, **30**, 092705.

[6]J. E. Ralph, J. S. Ross, A. B. Zylstra, A. L. Kritcher, H. F. Robey, C. V. Young, O. A. Hurricane, A. Pak, D. A. Callahan, K. L. Baker, D. T. Casey, T. Döppner, L. Divol, M. Hohenberger, S. L. Pape, P. K. Patel, R. Tommasini, S. J. Ali, P. A. Amendt, L. J. Atherton, B. Bachmann, D. Bailey, L. R. Benedetti, L. Berzak Hopkins, R. Betti, S. D. Bhandarkar, J. Biener, R. M. Bionta, N. W. Birge, E. J. Bond, D. K. Bradley, T. Braun, T. M. Briggs, M. W. Bruhn, P. M. Celliers, B. Chang, T. Chapman, H. Chen, C. Choate, A. R. Christopherson, D. S. Clark, J. W. Crippen, E. L. Dewald, T. R. Dittrich, M. J. Edwards, W. A. Farmer, J. E. Field, D. Fittinghoff, J. Frenje, J. Gaffney, M. Gatu Johnson, S. H. Glenzer, G. P. Grim, S. Haan, K. D. Hahn, G. N. Hall, B. A. Hammel, J. Harte, E. Hartouni, J. E. Heebner, V. J. Hernandez, H. W. Herrmann, M. C. Herrmann, D. E. Hinkel, D. D. Ho, J. P. Holder, W. W. Hsing, H. Huang, K. D. Humbird, N. Izumi, L. C. Jarrott, J. Jeet, O. Jones, G. D. Kerbel, S. M. Kerr, S. F. Khan, J. Kilkenny, Y. Kim, H. Geppert-Kleinrath, V. Geppert-Kleinrath, C. Kong, J. M. Koning, J. J. Kroll, M. K. G. Kruse, B. Kustowski, O. L. Landen, S. Langer, D. Larson, N. C. Lemos, J. D. Lindl, T. Ma, M. J. MacDonald, B. J. MacGowan, A. J. Mackinnon, S. A. MacLaren, A. G. MacPhee, M. M. Marinak, D. A. Mariscal, E. V. Marley, L. Masse, K. D. Meaney, N. B. Meezan, P. A. Michel, M. Millot, J. L. Milovich, J. D. Moody, A. S. Moore, J. W. Morton, T. J. Murphy, K. Newman, J.-M. G. Di Nicola, A. Nikroo, R. Nora, M. V. Patel, L. J. Pelz, J. L. Peterson, Y. Ping, B. B. Pollock, M. Ratledge, N. G. Rice, H. G. Rinderknecht, M. Rosen, M. S. Rubery, J. D. Salmonson, J. Sater, S. Schiaffino, D. J. Schlossberg, M. B. Schneider, C. R. Schroeder, H. A. Scott, S. M. Sepke, K. Sequoia, M. W. Sherlock, S. Shin, V. A. Smalyuk, B. K. Spears, P. T. Springer, M. Stadermann, S. Stoupin, D. J. Strozzi, L. J. Suter, C. A. Thomas, R. P. J. Town, C. Trosseille, E. R. Tubman, P. L. Volegov, C. R. Weber, K. Widmann, C. Wild, C. H. Wilde, B. M. Van Wonterghem, D. T. Woods, B. N. Woodworth, M. Yamaguchi, S. T. Yang, and G. B. Zimmerman, **15**, 2975.

[7]D. T. Bishel, B. Bachmann, A. Yi, D. Kraus, L. Divol, M. Bethkenhagen, R. W. Falcone, L. B. Fletcher, S. H. Glenzer, O. L. Landen, M. J. MacDonald, N. Masters, P. Neumayer, R. Redmer, A. M. Saunders, B. B. L. Witte, and T. Döppner, Review of Scientific Instruments **89**, 10G111 (2018).

[8]G. A. Kyrala, S. Dixit, S. Glenzer, D. Kalantar, D. Bradley, N. Izumi, N. Meezan, O. L. Landen, D. Callahan, S. V. Weber, J. P. Holder, S. Glenn, M. J. Edwards, P. Bell, J. Kimbrough, J. Koch, R. Prasad, L. Suter, J. L. Kline, and J. Kilkenny, Review of Scientific Instruments **81**, 10E316 (2010).

[9]B. Bachmann, S. MacLaren, S. Bhandarkar, T. Briggs, D. Casey, L. Divol, T. Döppner, D. Fittinghoff, M. Freeman, S. Haan, G. Hall, B. Hammel, E. Hartouni, N. Izumi, V. Geppert-Kleinrath, S. Khan, B. Kozioziemski, C. Krauland, O. Landen, D. Mariscal, E. Marley, L. Masse, K. Meaney, G. Mellos, A. Moore, A. Pak, P. Patel, M. Ratledge, N. Rice, M. Rubery, J. Salmonson, J. Sater, D. Schlossberg, M. Schneider, V. Smalyuk, C. Trosseille, P. Volegov, C. Weber, G. Williams, and A. Wray, Physical Review Letters **129**, 275001 (2022).

[10]L. C. Jarrott, L. R. Benedetti, H. Chen, N. Izumi, S. F. Khan, T. Ma, S. R. Nagel, O. L. Landen, A. Pak, P. K. Patel, M. Schneider, and H. A. Scott, Review of Scientific Instruments **87**, 11E534 (2016).

[11]D. A. Callahan, O. A. Hurricane, J. E. Ralph, C. A. Thomas, K. L. Baker, L. R. Benedetti, L. F. Berzak Hopkins, D. T. Casey, T. Chapman, C. E. Czajka, E. L. Dewald, L. Divol, T. Döppner, D. E. Hinkel, M. Hohenberger, L. C. Jarrott, S. F. Khan, A. L. Kritcher, O. L. Landen, S. LePape, S. A. MacLaren, L. P. Masse, N. B. Meezan, A. E. Pak, J. D. Salmonson, D. T. Woods, N. Izumi, T. Ma, D. A. Mariscal, S. R. Nagel, J. L. Kline, G. A. Kyrala, E. N. Loomis, S. A. Yi, A. B. Zylstra, and S. H. Batha, Physics of Plasmas **25**, 056305 (2018).

[12]O. L. Landen, J. Edwards, S. W. Haan, H. F. Robey, J. Milovich, B. K. Spears, S. V. Weber, D. S. Clark, J. D. Lindl, B. J. MacGowan, E. I. Moses, J. Atherton, P. A. Amendt, T. R. Boehly, D. K. Bradley, D. G. Braun, D. A. Callahan, P. M. Celliers, G. W. Collins, E. L. Dewald, L. Divol, J. A. Frenje, S. H. Glenzer, A. Hamza, B. A. Hammel, D. G. Hicks, N. Hoffman, N. Izumi, O. S. Jones, J. D. Kilkenny, R. K. Kirkwood, J. L. Kline, G. A. Kyrala, M. M. Marinak, N. Meezan, D. D. Meyerhofer, P. Michel, D. H. Munro, R. E. Olson, A. Nikroo, S. P. Regan, L. J. Suter, C. A. Thomas, and D. C. Wilson, Physics of Plasmas **18**, 051002 (2011).

[13]D. G. Hicks, B. K. Spears, D. G. Braun, R. E. Olson, C. M. Sorce, P. M. Celliers, G. W. Collins, and O. L. Landen, Physics of Plasmas **17**, 102703 (2010).

[14]A. L. Kritcher, A. B. Zylstra, D. A. Callahan, O. A. Hurricane, C. Weber, J. Ralph, D. T. Casey, A. Pak, K. Baker, B. Bachmann, S. Bhandarkar, J. Biener, R. Bionta, T. Braun, M. Bruhn, C. Choate, D. Clark, J. M. Di Nicola, L. Divol, T. Doeppner, V. Geppert-Kleinrath, S. Haan, J. Heebner, V. Hernandez, D. Hinkel, M. Hohenberger, H. Huang, C. Kong, S. Le Pape, D. Mariscal, E. Marley, L. Masse, K. D. Meaney, M. Millot, A. Moore, K. Newman, A. Nikroo, P. Patel, L. Pelz, N. Rice, H. Robey, J. S. Ross, M. Rubery, J. Salmonson, D. Schlossberg, S. Sepke, K. Sequoia, M. Stadermann, D. Strozzi, R. Tommasini, P. Volegov, C. Wild, S. Yang, C. Young, M. J. Edwards, O. Landen, R. Town, and M. Herrmann, Physics of Plasmas **28**,

		X-ray Data		Secondary DT-n Data			
Number	Name	P0 [um]	P2 [um]	σ_{AL} [ns]	σ_{SP} [ns]	σ_{NP} [ns]	σ_{EQ} [ns]
N161005	I_HDC_Sym_SubSc_S06a	61	9.27	21.96	20.95	25.31	19.31
N161031	I_HDC_Sym_AltFt_S01a	51.4	1.03	24.79	15.88	18.57	22.61
N161204	I_BigFt_Sym_540_S02a	60	11.22	22.41	18.85	23.32	11.73
N170201	I_HDC_Sym_ScaleTest_S01a	57.7	-11.54	15.76	9.96	9.44	13.81
N170205	I_HDC_Sym_ScaleTest_S02a	53.7	-18.26	25.89	15.02	17.27	25.04
N170206	I_HDC_Sym_ScaleTest_S04a	58.4	-7.36	25.16	15.29	18.11	23.18
N170320	I_HDC_Sym_AltFt_S02a	51.4	1.03	23.83	14.42	16.76	18.87
N170327	I_Be_Sym_CCR_S01a	61.4	8.60	25.02	19.91	23.31	19.94
N170330	I_BigFt_Sym_ScaleTest_S01a	64.3	-2.25	13.72	14.37	14.57	9.77
N170406	I_Be_Sym_CCR_S02a	56.3	6.47	22.71	20.91	23.47	20.76
N170417	I_HDC_Sym_ScaleTest_S07a	67.2	-0.67	22.43	16.15	18.70	19.34
N170503	I_Be_Sym_CCR_S05a	56.3	-2.82	29.31	15.86	19.55	24.66
N170530	I_Be_Sym_CCR_S04a	52.5	11.34	25.18	22.17	27.72	17.41
N170702	I_HDC_Sym_ScaleTest_S08a	67.2	-0.67	23.28	18.33	21.67	20.38
N170925	I_Int_Sym_P5_S03b	67.2	-0.67	21.66	18.40	22.67	18.67
N170926	I_Int_Sym_P5_S02b	64.1	9.49	19.88	18.90	24.09	17.70
N170927	I_Cap_Sym_KBEmit_S03a	56.9	-3.07	25.48	14.01	18.11	21.17
N171226	I_Be_Sym_IBProp_S03a	52.5	11.34	22.68	15.65	18.23	20.12
N171226	I_Be_Sym_IBProp_S01a	52.5	11.34	19.67	20.22	22.78	17.06
N171227	I_Be_Sym_IBProp_S02a	52.5	11.34	21.94	13.70	15.61	20.18
N180102	I_Hohl_SymWalMo_Abl_S01a	77	-16.94	10.19	14.04	14.56	13.39
N180305	I_Cap_Sym_TiltKBEmit_S01a	56.9	0.00	18.63	13.06	17.69	17.18
N180305	I_Cap_Sym_KBEmit_S04a	56.9	-3.07	25.12	15.98	19.44	22.09
N180319	I_Int_Sym_HyB_S04a	60.3	31.96	19.59	21.25	24.97	16.55
N180509	I_Hohl_Sym_Iraum_S01a	73.5	31.24	19.13	14.64	21.27	17.08
N180619	I_Int_Sym_HyC_S05a	48.2	5.30	15.46	13.31	19.04	13.33
N180619	Fa_Calib_Sym_StdCndle_S06a	46.1	-7.05	12.91	12.76	14.25	14.89
N180626	I_Int_Sym_HyC_S06c	48.2	5.30	12.08	13.90	13.34	8.87
N180702	I_Hohl_Sym_Cyl_S02a	60.6	-24.24	21.06	13.91	19.63	21.78
N180705	I_Hohl_SymWalMo_ThnWll_S12a	66.7	-11.34	12.94	12.65	18.24	17.92
N180830	I_Hohl_Sym_Iraum_S03a	60.3	1.81	19.00	14.36	15.16	12.43
N181113	I_Hohl_Sym_Iraum_S04a	71.1	-1.42	17.27	12.89	14.12	10.45
N181114	I_Hohl_Sym_FOAM_S08a	71.1	-1.42	20.46	14.67	9.25	9.75
N181114	I_Hohl_Sym_FOAM_S10a	54.3	-5.38	14.01	13.02	14.51	19.20
N181210	I_Cap_Sym_KBEmit_S06a	57.4	-2.64	22.32	13.89	17.96	22.60
N190204	I_Hohl_Sym_Frust_S01b	73.5	31.24	15.64	16.19	17.11	11.58
N190206	I_Hohl_Sym_FOAM_S09b	62.1	-6.52	18.10	11.93	16.23	21.41
N190218	I_Int_Sym_HyE_S01a	64.9	-32.45	23.82	11.09	13.70	20.26
N190219	I_Cap_Sym_KBEmit_S08a	57.4	-2.64	15.17	16.63	18.90	17.34
N190226	I_Cap_Sym_KBInrShl_S02a	49.4	-7.31	19.53	12.89	14.49	19.29
N190417	I_Hohl_Sym_Frust_S02a	57	-38.19	19.66	7.45	10.13	23.33
N190505	I_Int_Sym_HyE_S04a	76.5	15.30	19.01	18.77	23.68	15.09
N190520	I_Hohl_Sym_Frust_S03a	51	-34.68	16.52	8.87	11.32	19.59
N190610	Fa_Calib_Sym_StdCndle_S08a	49.8	0.60	19.87	13.41	18.88	15.45
N190826	I_Int_Sym_HyE_S07a	77.5	-5.19	19.60	14.19	17.38	18.99
N190903	I_Int_Sym_2Shk_S01a	53	0.42	20.45	18.50	22.04	19.81
N200217	I_DPI_Sym_Frust_S01a	83	21.58	16.37	18.82	20.89	16.38
N201018	I_DPI_Sym_Frust_S03a	94	0.94	19.77	15.33	18.61	18.88
N210125	I_Int_Sym_HohlScan_S01a	70.1	2.59	19.18	15.29	18.32	16.37
N210329	I_DPI_Sym_Frust_S05a	75.5	-19.63	21.23	13.93	15.99	20.68
N210404	I_Int_Sym_HohlScan_S03a	70.1	-4.91	21.50	15.77	18.37	19.00
N210608	I_DPI_Sym_Frust_S06b	78.9	-10.65	21.78	16.50	19.68	18.95
N210614	I_Int_Sym_HohlScan_S04a	84.2	1.68	21.89	17.36	20.70	20.10
N210724	I_DPI_Sym_Frust_S08a	88.9	39.65	19.72	21.70	26.21	15.21
N210912	I_Hohl_Sym_LEHHware_S02a	68.4	-9.58	21.08	15.09	19.23	20.18
N210928	I_Hohl_Sym_LEHHware_S03a	79.6	6.77	21.77	18.05	22.17	19.29
N211226	I_Adia_Sym_SQN_S01a	48.2	-26.51	21.82	13.78	16.71	19.58
N220222	I_DPI_Sym_BPhase_S02a	44.6	-6.33	16.62	16.29	19.71	13.99
N220410	I_Stag_Sym_HyEMerge_S01a	59.8	0.54	17.68	14.28	17.12	15.69
N220703	I_Stag_Sym_HyECpl_S02a	64.5	-18.71	23.13	14.16	16.09	21.89

TABLE II. Table detailing the data set that comprise this work.

072706 (2021).
[15]B. Bachmann, J. E. Ralph, A. B. Zylstra, S. A. MacLaren, T. Döppner, D. O. Gericke, G. W. Collins, O. A. Hurricane, T. Ma, J. R. Rygg, H. A. Scott, S. A. Yi, and P. K. Patel, Physical Review E **101**, 033205 (2020).
[16]D. S. Clark, M. M. Marinak, C. R. Weber, D. C. Eder, S. W. Haan, B. A. Hammel, D. E. Hinkel, O. S. Jones, J. L. Milovich, P. K. Patel, H. F. Robey, J. D. Salmonson, S. M. Sepke, and C. A. Thomas, Physics of Plasmas **22**, 022703 (2015).
[17]R. H. H. Scott, D. S. Clark, D. K. Bradley, D. A. Callahan, M. J. Edwards, S. W. Haan, O. S. Jones, B. K. Spears, M. M. Marinak, R. P. J. Town, P. A. Norreys, and L. J. Suter, **110**, 075001.
[18]H. G. Rinderknecht, M. J. Rosenberg, A. B. Zylstra, B. Lahmann, F. H. Séguin, J. A. Frenje, C. K. Li, M. Gatu Johnson, R. D. Petrasso, L. F. Berzak Hopkins, J. A. Caggiano, L. Divol, E. P. Hartouni, R. Hatarik, S. P. Hatchett, S. Le Pape, A. J. Mackinnon, J. M. McNaney, N. B. Meezan, M. J. Moran, P. A. Bradley, J. L. Kline, N. S. Krasheninnikova, G. A. Kyrala, T. J. Murphy, M. J. Schmitt, I. L. Tregillis, S. H. Batha, J. P. Knauer, and J. D. Kilkenny, Physics of Plasmas **22**, 082709 (2015).
[19]V. Y. Glebov, T. C. Sangster, C. Stoeckl, J. P. Knauer, W. Theobald, K. L. Marshall, M. J. Shoup, T. Buczek, M. Cruz, T. Duffy, M. Romanofsky, M. Fox, A. Pruyne, M. J. Moran, R. A. Lerche, J. McNaney, J. D. Kilkenny, M. J. Eckart, D. Schneider, D. Munro, W. Stoeffl, R. Zacharias, J. J. Haslam, T. Clancy, M. Yeoman, D. Warwas, C. J. Horsfield, J.-L. Bourgade, O. Landoas, L. Disdier, G. A. Chandler, and R. J. Leeper, Review of Scientific Instruments **81**, 10D325 (2010).
[20]R. Hatarik, J. A. Caggiano, V. Glebov, J. McNANEY, C. Stoeckl, and D. H. G. Schneider, Plasma and Fusion Research **9**, 4404104 (2014).
[21]C. Cerjan, D. B. Sayre, and S. M. Sepke, Physics of Plasmas **25**, 022705 (2018).
[22]B. Lahmann, en*Using fusion-product spectroscopy to diagnose inertial confinement fusion implosions and study stopping power on OMEGA, the NIF, and Z*, Thesis, Massachusetts Institute of Technology (2021), accepted: 2022-01-14T15:19:54Z.
[23]S. A. Slutz, M. C. Herrmann, R. A. Vesey, A. B. Sefkow, D. B. Sinars, D. C. Rovang, K. J. Peterson, and M. E. Cuneo, Physics of Plasmas **17**, 056303 (2010), publisher: American Institute of Physics.
[24]M. Gomez, S. Slutz, A. Sefkow, D. Sinars, K. Hahn, S. Hansen, E. Harding, P. Knapp, P. Schmit, C. Jennings, T. Awe, M. Geissel, D. Rovang, G. Chandler, G. Cooper, M. Cuneo, A. Harvey-Thompson, M. Herrmann, M. Hess, O. Johns, D. Lamppa, M. Martin, R. McBride, K. Peterson, J. Porter, G. Robertson, G. Rochau, C. Ruiz, M. Savage, I. Smith, W. Stygar, and R. Vesey, Physical Review Letters **113**, 155003 (2014).
[25]P. Schmit, P. Knapp, S. Hansen, M. Gomez, K. Hahn, D. Sinars, K. Peterson, S. Slutz, A. Sefkow, T. Awe, E. Harding, C. Jennings, G. Chandler, G. Cooper, M. Cuneo, M. Geissel, A. Harvey-Thompson, M. Herrmann, M. Hess, and R. Vesey, Physical review letters **113**, 155004 (2014).
[26]P. F. Knapp, P. F. Schmit, S. B. Hansen, M. R. Gomez, K. D. Hahn, D. B. Sinars, K. J. Peterson, S. A. Slutz, A. B. Sefkow, T. J. Awe, E. Harding, C. A. Jennings, M. P. Desjarlais, G. A. Chandler, G. W. Cooper, M. E. Cuneo, M. Geissel, A. J. Harvey-Thompson, J. L. Porter, G. A. Rochau, D. C. Rovang, C. L. Ruiz, M. E. Savage, I. C. Smith, W. A. Stygar, and M. C. Herrmann, Physics of Plasmas **22**, 056312 (2015).
[27]K. D. Hahn, G. A. Chandler, C. L. Ruiz, G. W. Cooper, M. R. Gomez, S. Slutz, A. B. Sefkow, D. B. Sinars, S. B. Hansen, P. F. Knapp, P. F. Schmit, E. Harding, C. A. Jennings, T. J. Awe, M. Geissel, D. C. Rovang, J. A. Torres, J. A. Bur, M. E. Cuneo, V. Y. Glebov, A. J. Harvey-Thompson, M. C. Herrman, M. H. Hess, O. Johns, B. Jones, D. C. Lamppa, J. S. Lash, M. R. Martin, R. D. McBride, K. J. Peterson, J. L. Porter, J. Reneker, G. K. Robertson, G. A. Rochau, M. E. Savage, I. C. Smith, J. D. Styron, and R. A. Vesey, Journal of Physics: Conference Series **717**, 012020 (2016).
[28]W. E. Lewis, P. F. Knapp, S. A. Slutz, P. F. Schmit, G. A. Chandler, M. R. Gomez, A. J. Harvey-Thompson, M. A. Mangan, D. J. Ampleford, and K. Beckwith, Physics of Plasmas **28**, 092701 (2021).
[29]J. Moody, B. Pollock, H. Sio, D. Strozzi, D. Ho, C. Walsh, G. Kemp, S. Kucheyev, B. Kozioziemski, E. Carroll, J. Kroll, D. Yanagisawa, J. Angus, S. Bhandarkar, J. Bude, L. Divol, B. Ferguson, J. Fry, L. Hagler, and S. Fujioka, Journal of Fusion Energy **41** (2022), 10.1007/s10894-022-00319-7.
[30]H. Sio, J. D. Moody, D. D. Ho, B. B. Pollock, C. A. Walsh, B. Lahmann, D. J. Strozzi, G. E. Kemp, W. W. Hsing, A. Crilly, J. P. Chittenden, and B. Appelbe, Review of Scientific Instruments **92**, 043543 (2021), publisher: American Institute of Physics.
[31]L. Ballabio, J. Källne, and G. Gorini, Nuclear Fusion **38**, 1723 (1998).
[32]L. S. Brown, D. L. Preston, and R. L. Singleton Jr., Physics Reports **410**, 237 (2005).
[33]P. J. Adrian, R. Florido, P. E. Grabowski, R. Mancini, B. Bachmann, L. X. Benedict, M. G. Johnson, N. Kabadi, B. Lahmann, C. K. Li, R. D. Petrasso, H. G. Rinderknecht, S. P. Regan, F. H. Séguin, R. L. Singleton, H. Sio, G. D. Sutcliffe, H. D. Whitley, and J. A. Frenje, Physical Review E **106**, L053201 (2022).
[34]N. Jarmie, R. E. Brown, and R. A. Hardekopf, **29**, 2031.
[35]Z. L. Mohamed, O. M. Mannion, E. P. Hartouni, J. P. Knauer, and C. J. Forrest, **128**, 214501.
[36]J. A. Brown, B. L. Goldblum, L. A. Bernstein, D. L. Bleuel, N. M. Brickner, J. A. Caggiano, B. H. Daub, G. S. Kaufman, R. Hatarik, T. W. Phillips, S. A. Wender, K. van Bibber, J. Vujic, and N. P. Zaitseva, Journal of Applied Physics **115**, 193504 (2014).
[37]B. Bachmann, T. Hilsabeck, J. Field, N. Masters, C. Reed, T. Pardini, J. R. Rygg, N. Alexander, L. R. Benedetti, T. Döppner, A. Forsman, N. Izumi, S. LePape, T. Ma, A. G. MacPhee, S. Nagel, P. Patel, B. Spears, and O. L. Landen, Review of Scientific Instruments **87**, 11E201 (2016).
[38]A. S. Moore, E. P. Hartouni, D. Schlossberg, S. Kerr, M. Eckart, J. Carrera, L. Ma, C. Waltz, D. Barker, J. Gjemso, E. Mariscal, G. Grim, and J. Kilkenny, Review of Scientific Instruments **92**, 023516 (2021).
[39]A. L. Kritcher, C. V. Young, H. F. Robey, C. R. Weber, A. B. Zylstra, O. A. Hurricane, D. A. Callahan, J. E. Ralph, J. S. Ross, K. L. Baker, D. T. Casey, D. S. Clark, T. Döppner, L. Divol, M. Hohenberger, L. B. Hopkins, S. Le Pape, N. B. Meezan, A. Pak, P. K. Patel, R. Tommasini, S. J. Ali, P. A. Amendt, L. J. Atherton, B. Bachmann, D. Bailey, L. R. Benedetti, R. Betti, S. D. Bhandarkar, J. Biener, R. M. Bionta, N. W. Birge, E. J. Bond, D. K. Bradley, T. Braun, T. M. Briggs, M. W. Bruhn, P. M. Celliers, B. Chang, T. Chapman, H. Chen, C. Choate, A. R. Christopherson, J. W. Crippen, E. L. Dewald, T. R. Dittrich, M. J. Edwards, W. A. Farmer, J. E. Field, D. Fittinghoff, J. A. Frenje, J. A. Gaffney, M. G. Johnson, S. H. Glenzer, G. P. Grim, S. Haan, K. D. Hahn, G. N. Hall, B. A. Hammel, J. Harte, E. Hartouni, J. E. Heebner, V. J. Her-

nandez, H. Herrmann, M. C. Herrmann, D. E. Hinkel, D. D. Ho, J. P. Holder, W. W. Hsing, H. Huang, K. D. Humbird, N. Izumi, L. C. Jarrott, J. Jeet, O. Jones, G. D. Kerbel, S. M. Kerr, S. F. Khan, J. Kilkenny, Y. Kim, H. Geppert-Kleinrath, V. Geppert-Kleinrath, C. Kong, J. M. Koning, M. K. G. Kruse, J. J. Kroll, B. Kustowski, O. L. Landen, S. Langer, D. Larson, N. C. Lemos, J. D. Lindl, T. Ma, M. J. MacDonald, B. J. MacGowan, A. J. Mackinnon, S. A. MacLaren, A. G. MacPhee, M. M. Marinak, D. A. Mariscal, E. V. Marley, L. Masse, K. Meaney, P. A. Michel, M. Millot, J. L. Milovich, J. D. Moody, A. S. Moore, J. W. Morton, T. Murphy, K. Newman, J.-M. G. Di Nicola, A. Nikroo, R. Nora, M. V. Patel, L. J. Pelz, J. L. Peterson, Y. Ping, B. B. Pollock, M. Ratledge, N. G. Rice, H. Rinderknecht, M. Rosen, M. S. Rubery, J. D. Salmonson, J. Sater, S. Schiaffino, D. J. Schlossberg, M. B. Schneider, C. R. Schroeder, H. A. Scott, S. M. Sepke, K. Sequoia, M. W. Sherlock, S. Shin, V. A. Smalyuk, B. K. Spears, P. T. Springer, M. Stadermann, S. Stoupin, D. J. Strozzi, L. J. Suter, C. A. Thomas, R. P. J. Town, C. Trosseille, E. R. Tubman, P. L. Volegov, K. Widmann, C. Wild, C. H. Wilde, B. M. Van Wonterghem, D. T. Woods, B. N. Woodworth, M. Yamaguchi, S. T. Yang, and G. B. Zimmerman, Nature Physics **18**, 251 (2022).

[40] A. B. Zylstra, A. L. Kritcher, O. A. Hurricane, D. A. Callahan, J. E. Ralph, D. T. Casey, A. Pak, O. L. Landen, B. Bachmann, K. L. Baker, L. Berzak Hopkins, S. D. Bhandarkar, J. Biener, R. M. Bionta, N. W. Birge, T. Braun, T. M. Briggs, P. M. Celliers, H. Chen, C. Choate, D. S. Clark, L. Divol, T. Döppner, D. Fittinghoff, M. J. Edwards, M. Gatu Johnson, N. Gharibyan, S. Haan, K. D. Hahn, E. Hartouni, D. E. Hinkel, D. D. Ho, M. Hohenberger, J. P. Holder, H. Huang, N. Izumi, J. Jeet, O. Jones, S. M. Kerr, S. F. Khan, H. Geppert Kleinrath, V. Geppert Kleinrath, C. Kong, K. M. Lamb, S. Le Pape, N. C. Lemos, J. D. Lindl, B. J. MacGowan, A. J. Mackinnon, A. G. MacPhee, E. V. Marley, K. Meaney, M. Millot, A. S. Moore, K. Newman, J.-M. G. Di Nicola, A. Nikroo, R. Nora, P. K. Patel, N. G. Rice, M. S. Rubery, J. Sater, D. J. Schlossberg, S. M. Sepke, K. Sequoia, S. J. Shin, M. Stadermann, S. Stoupin, D. J. Strozzi, C. A. Thomas, R. Tommasini, C. Trosseille, E. R. Tubman, P. L. Volegov, C. R. Weber, C. Wild, D. T. Woods, S. T. Yang, and C. V. Young, Physical Review E **106**, 025202 (2022).

[41] M. D. Cable and S. P. Hatchett, Journal of Applied Physics **62**, 2233 (1987).

[42] M. D. Cable, S. P. Hatchett, and M. B. Nelson, Review of Scientific Instruments **63**, 4823 (1992).

[43] The R^2 was computed as follows. $R^2 = 1 - \sum_i (y^i - y^i_{MCM})^2 / \sum_i (y^i_{MCM} - \hat{y}^i_{MCM})^2$ where y^i is the σ_{SQ}/σ_{NP} of the data and yi_{MCM} is the σ_{SQ}/σ_{NP} predicted by the MCM. The value $\hat{y}^i_{MCM}$ is the mean of all σ_{SQ}/σ_{NP} predicted by the model.

[44] S. H. Langer, I. Karlin, and M. M. Marinak, English"Performance Characteristics of HYDRA - a Multi-Physics simulation code from Lawrence Livermore National Laboratory," Tech. Rep. LLNL-TR-648439 (Lawrence Livermore National Lab. (LLNL), Livermore, CA (United States), 2014).